THE MICROSCOPE • Vol 58:4, pp 147-158 (2010)

SEM Characterization of Epitaxially Grown Aluminum Oxide Employed as Sensor Substrates[1]

Martin Kocanda and Bryn M. Wilke
Northern Illinois University*

KEYWORDS

Anodic aluminum oxide (AAO), atomic force microscopy (AFM), crystallography, epitaxial growth, films, nanoporous, nucleation, scanning electron microscopy (SEM), sensor, volatile organic compounds (VOCs)

ABSTRACT

Anodic aluminum oxide (AAO) films have been used as protective coatings since the 1950s and more recently as a decorative metallic finish. The porosity, surface morphology and fabrication methods of these films have been studied extensively. Common to the commercial AAO films is the anodization process of aluminum fabricated in the (100) crystallographic plane using inorganic electrolytes. A more recent application of this anodic process, using low solubility salts, has been the fabrication of hexagonal templates to grow domains of nanowires and nanotubes.

The use of microelectronic fabrication methods to epitaxially grow (111) aluminum thin films, and the subsequent anodization method, has been recently employed to implement nanostructured AAO materials as commercial moisture sensors and as substrates to study the adsorption response of volatile organic compounds (VOCs) and biochemical compounds. These epitaxially grown films contain nanoporous structures having pore morphologies similar to the (100) film but appear to grow radially from the tetrahedral and hexagonal domains. In this work, the surface morphology of epitaxially grown porous nanostructures is elucidated using scanning electron microscopy (SEM) and atomic force microscopy (AFM).

INTRODUCTION

Experimentation during the last decade of the 19th century described the protective nature of anodic aluminum films (1). Little was known, however, about the oxide surface morphology until advanced microscopy techniques such as SEM were developed. The porous nature of the oxide films was exploited during the 1950s, when colorization was extensively researched and patented. A two-step method employed anodization in sulfuric acid, followed by an alternating current anodization in a solution containing metal salts (2). Later refinements to the process proved commercially successful. Commercial household products typically developed during this decade were aluminum siding and gutters. Consumer goods containing protective and decorative anodic finishes have since proliferated among many products commonly found in the typical household.

The advent of electron microscopy allowed the porous nature of AAO films to be extensively researched. The work of Keller et al. described the porous morphology consisting of uniformly spaced hexagonal structures using SEM techniques (3). Subsequent work had also described the relationship between the anodization potential and the interpore distance (4).

The common trade name of generic aluminum oxide is *alumina* and is used extensively in the literature.

[1]Presented at Inter/Micro 2010, Chicago.
*College of Engineering and Engineering Technology, NIU, DeKalb, IL 60115

Table 1. Six Forms of Aluminum Oxide (5, 8)

Formula	Name	System	ρ (g/cm³)	Comments
α-Al_2O_3	Corundum	hexagonal	3.97	abundant natural oxide
α-$Al_2O_3 \cdot H_2O$	Boehmite	orthorhombic	3.44	
α-$Al_2O_3 \cdot 3H_2O$	Gibbsite	monoclinic	2.42	alternate: $Al(OH)_3$
β-$Al_2O_3 \cdot 3H_2O$	Diaspore	orthorhombic	3.40	
β-$Al_2O_3 \cdot 3H_2O$	Bayerite	monoclinic	2.53	
γ-$Al_2O_3 \cdot 3H_2O$	Gamma alumina	amorphous	—	

There are six known polymorphs of alumina (Table 1); all are commonly known by their mineralogical classification. Two of these exist as hydrates of the alpha form, and two exist as hydrates of the beta form (5). Corundum (α-Al_2O_3) occurs abundantly in nature. Substitution of the aluminum ion in the crystal lattice with trivalent ions results in polymorphs with a variety of optical properties. Sapphire and ruby are common occurrences of such substitution polymorphs where trace amounts of iron, titanium or chromium are substituted (5). Gamma alumina (γ-Al_2O_3) is the amorphous form of corundum. It is not abundant in a natural state. Two hydrated forms of alpha alumina are boehmite (α-$Al_2O_3 \cdot H_2O$) and gibbsite (α-$Al_2O_3 \cdot 3H_2O$). The two hydrated forms of beta alumina are diaspore (β-$Al_2O_3 \cdot H_2O$) and bayerite (β-$Al_2O_3 \cdot 3H_2O$). Note that the dihydrates of the alpha and beta forms do not exist.

Corundum is the most thermodynamically stable form of alumina. This form is generated at temperatures above 1100 °C and is independent of the transition path. Gamma alumina is formed by dehydration of boehmite, typically at 400 °C to 500 °C.

The formation of aluminum oxide (α-Al_2O_3) usually occurs by two synthesis pathways. The commonly known pathways include oxidation in atmospheric oxygen (O_2) and electrolytic oxidation. Each is thermodynamically favorable as indicated by the large negative free energy (6):

$$2Al + 3/2O_2 \rightarrow \alpha\text{-}Al_2O_3$$
$$\Delta G° = -1582 \text{ kJ/mol} \qquad \text{Eq. 1}$$

$$2Al + 3H_2O \rightarrow \alpha\text{-}Al_2O_3 + 3H_2(g)$$
$$\Delta G° = -871 \text{ kJ/mol} \qquad \text{Eq. 2}$$

The net electrolytic reaction involves the transfer of six electrons. The anodic reaction is:

$$2Al + 3H_2O \rightarrow Al_2O_3 + 6H^+ + 6e^- \qquad \text{Eq. 3}$$

The cathodic reaction is:

$$6H^+ + 6e^- \rightarrow 3H_2(g) \qquad \text{Eq. 4}$$

The thermodynamics of the reaction is governed by the Nernst equation:

$$E = E° - \frac{RT}{nF} \ln \frac{(red)}{(ox)} \qquad \text{Eq. 5}$$

where R is the universal gas constant (8.314 kJ/mol/K), T is the absolute temperature (K), n is the number of electrons transferred, F is the Faraday constant (96,485 C/mol), *red* is the concentration of the reduced species and *ox* is the concentration of the oxidized species.

The above equations are an oversimplification, to a lesser extent, in describing the electrolytic alumina synthesis. A number of variables influence the type of oxide film and the degree of complexity or ordering of the film. In particular, the electrolyte offers a significant contribution to the formation of the film structure. The electrolytic oxidation of aluminum produces two types of films (Figure 1). A barrier type film, devoid of nanopores, is synthesized using partially soluble electrolytes in a mildly acidic pH range; nanoporous films are synthesized using a slightly soluble electrolyte (7).

Barrier film synthesis occurs when the pH is controlled (pH 5 to 7) using neutral boric acid, ammonium borate, ammonium tartrate, or ammonium tetraborate in ethylene glycol. Organic acids including citric acid, malic acid and glycolic acid may also be employed. Boric acid, however, does not dissociate in aqueous solution. It is acidic due to its interaction (solvation) with water forming the tetrahydroxyborate ion:

$$B(OH)_3 + H_2O \rightarrow B(OH)_4^- + H^+ \qquad \text{Eq. 6}$$

The K_a and pK_a of boric acid are 5.8×10^{-10} and 9.24 respectively (8). Because barrier films are compact and

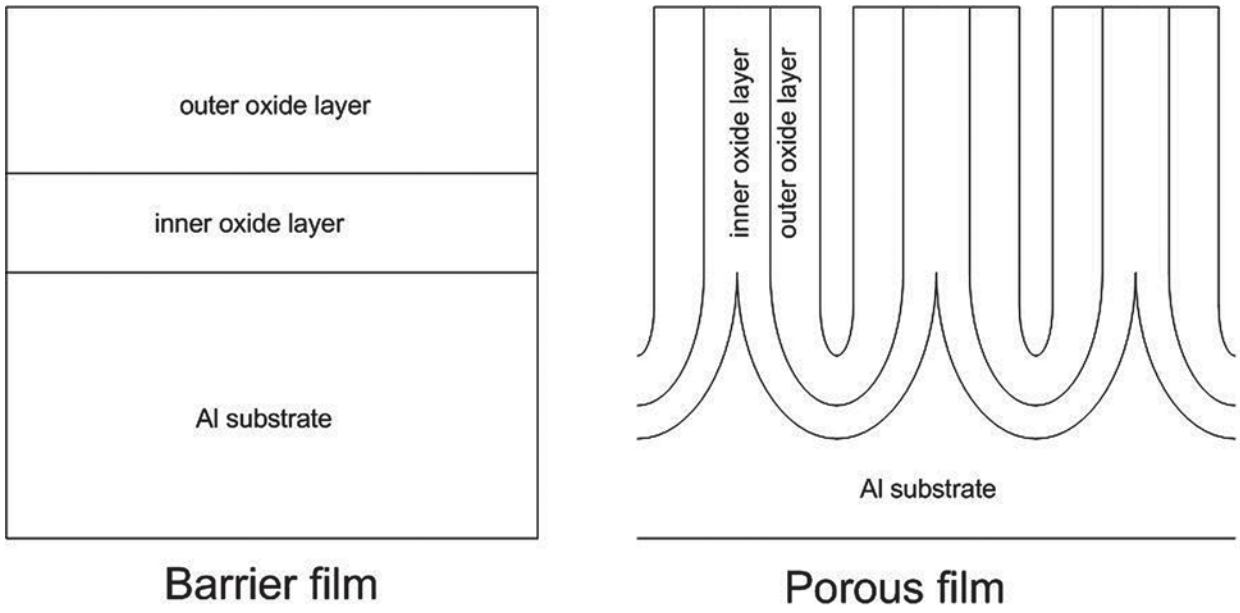

Figure 1. Comparison of barrier film versus porous oxide depicting cross-section of layers. The aluminum substrate is the starting material, the inner oxide layer is composed of pure alumina and the outer layer is composed of alumina containing anionic species.

Table 2. Comparison of Anodizing Ratios and Electrolytes*

Electrolyte composition	T (°C)	nm/V
10% (V/V) sulfuric acid (H_2SO_4)	10	1.00
2% (V/V) oxalic acid $(COOH)_2$	24	1.18
4% phosphoric acid (H_3PO_4)	24	1.19
3% chromic acid (H_2CrO_4)	38	1.25

*Anodizing ratio (nm/V) for the barrier layer as found underlying the porous outer layer and overlying the metal substrate (7).

durable, they are typically employed as dielectric layers in capacitors.

Synthesis of porous aluminum is typically performed under moderately strong acidic conditions using electrolytes containing soluble salts (7). The details of pore formation have been widely studied and it has been demonstrated that the interpore spacing and pore diameters are affected by the type of acid and anodization potential (6, 8). The typical electrolytes employed in nanoporous AAO synthesis are sulfuric acid, oxalic acid, chromic acid and phosphoric acid (7). A recent investigation of other electrolytes to control the interpore distance and pore diameter has been performed (9, 10). Malonic acid and tartaric acid were employed in the investigation resulting in pore distances and diameters intermediate to oxalic acid and phosphoric acid.

The thickness of porous films is time dependent; the thickness of barrier films is voltage dependent. Therefore, porous films may be grown to thicknesses much larger than barrier films. Consideration of other factors in the synthesis of porous film must be made. The time and current density are a common concern; however, the electrolyte temperature and composition affects the film density (7). At low temperatures (0 °C to 5 °C), thick, compact and hard films are produced. This is commonly known as hard anodization. At high temperatures, typically above ambient (60 °C to 75 °C), thin, non-protective and soft films are formed. Therefore, the soft anodization process has been named accordingly.

Porous AAO films consist of two layers. The inner layer is thin and compact without pores, resembling barrier-type oxide. The overlying layer is thick and porous. An upper limit on the thickness of the inner barrier layer may be estimated considering the elec-

Table 3. Comparison of Pore Diameter and Electrolytes*

Electrolyte composition	T (°C)	Pore diameter (nm)
10% (V/V) sulfuric acid (H_2SO_4)	10	12.0
2% (V/V) oxalic acid $(COOH)_2$	24	17.0
3% chromic acid (H_2CrO_4)	38	24.0
4% phosphoric acid (H_3PO_4)	24	33.0

*Cylindrical pore diameter measurements as noted by Keller, et al. as a function of electrolyte composition at specified temperature and independent of anodization potential (3).

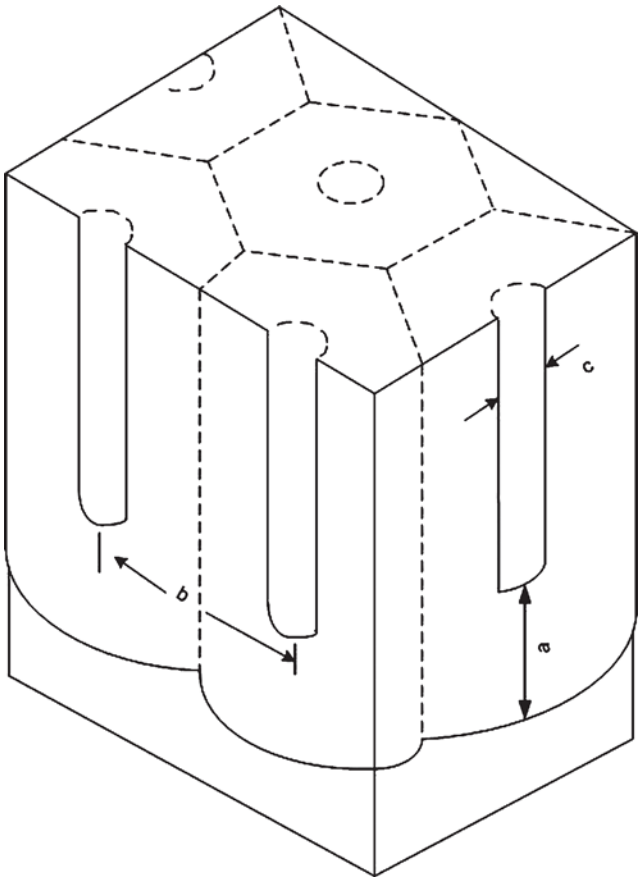

Figure 2. Typical cylindrical AAO cross-section. The commonly referenced AAO parameters are barrier layer thickness (a), interpore spacing (b) and pore diameter (c).

trolyte composition and the anodization potential (Table 2). The anodizing ratio defines the thickness per unit potential applied during the process.

Pore formation mechanisms and the pore morphology have been studied extensively since the 1950s (6). Subsequent studies attempt to explain the influence of the electric field on the migration of anions to the aluminum surface and the migration of cations through the barrier oxide region and, therefore, the shape of the pores as influenced by the electric field. As previously noted, the electrolyte composition and anodization potential influence the oxide properties. Further related studies have elucidated the effects of the electrolyte and anodization potential on the pore formation.

Two pore morphologies have been noted in the literature: cylindrical and hexagonal. Cylindrical-shaped pores were studied in detail by Keller, Hunter and Robinson using four common electrolytes (3). The pore diameters were influenced by the electrolytes. Using 4% phosphoric acid, 33 nm diameter pores were produced; 3% chromic acid produced 24 nm diameter pores; 2% oxalic produced 17 nm diameter pores and 15% sulfuric acid produced 12 nm diameter pores (Table 3). Three pore dimensions that are commonly referenced are a) the barrier layer thickness, b) interpore spacing (or pore wall thickness) and c) the pore diameter (Figure 2). This figure depicts the ideal nanopore structure; specifically, the cells are hexagonal with cylindrical symmetric pores. However, typical nanopore structures deviate from the idea, because some symmetry, such as the pore diameters, vary and the pores do not always have perfect cylindrical shapes.

Measurements of the pore wall dimensions were performed by Keller concurrently with the pore diameter study. The pore wall thickness (and implicitly the interpore distance) was found to be proportional to the pore diameter (Table 4). Included in the study was the relationship between the pore density and the anodization potential. As the potential is increased, the volume of the cell oxide increases, resulting in a decreased number of pores per unit area. This relationship may be expressed such that the pore density per unit area decreases inversely with the anodization potential (Table 5).

Current density must be considered during the synthesis of nanoporous structures. Variations in the

Table 4. Comparison of Wall Diameters and Electrolytes*

Electrolyte composition	T (°C)	Wall diameter (nm/V)
10% (V/V) sulfuric acid (H_2SO_4)	10	8.0
2% (V/V) oxalic acid $(COOH)_2$	24	9.7
3% chromic acid (H_2CrO_4)	38	10.9
4% phosphoric acid (H_3PO_4)	24	11.0

*Cylindrical wall anodizing ratio as noted by Keller, et al. as a function of electrolyte composition at specified temperature and dependent on anodization potential (3).

Table 5. Comparison of Pore Densities and Anodization Potentials*

Anodization potential (V)	Pore density (x 10^9 cm^{-2})
15	83
20	56
30	30

*Pore density as noted by Keller, et al. as a function of anodization potential (3). The pore density is in number per unit area. Experimental results were observed in AAO film formed from anodization in 15% sulfuric acid at 10 °C and at constant current density.

Table 6. Comparison of Pore Diameter and Anodization Conditions*

J (mA cm^{-2})	Time (minutes)	Pore base diameter (nm)	Pore mouth diameter (nm)
10	30	12.0	15.9
15	30	12.0	18.2
15	60	12.0	24.6
25	30	12.0	20.8

*Variations in the pore diameters (base diameter compared to mouth diameter) as noted by Paolini et al. as a function of time and current density (11). Experimental results were observed in AAO film formed from anodization in 20% sulfuric acid at 10 °C and at constant anodization potential.

pore geometry as a function of current density were first proposed by Keller (3) and subsequently confirmed by Paolini (11). The studies have shown that the pore resembles a truncated cone rather than a cylinder with parallel sides. The base diameter of the pore, located at the barrier layer adjacent to the aluminum metal, is slightly narrower than the mouth, which is located at the open end of the pore. The studies were performed using 20% sulfuric acid with variations in the current density and anodization time (Table 6). A consequence of the pore widening effect is that there will be a maximum theoretical limit on the thickness of the porous oxide layer. As the pore continues its growth (away from the base metal), the pore widens until the walls of the adjacent cell converge. Beyond this point, no wall formation can occur (7).

The basis for all of the experimental work cited above (including the initial conditions) was that an electropolished (100) aluminum base metal was employed. The electropolishing solution typically con-

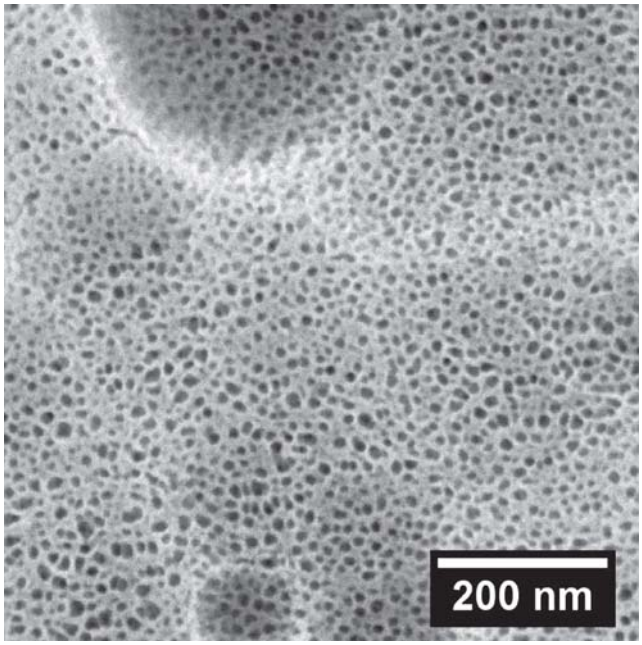

Figure 3. SEM image of reduced-symmetry AAO structures. Relaxation of controls during the anodization process typically produces less ordering and symmetry in AAO structures (13). Note the planarity of the nanoporous film; the oxide film was grown on (100) aluminum sheet.

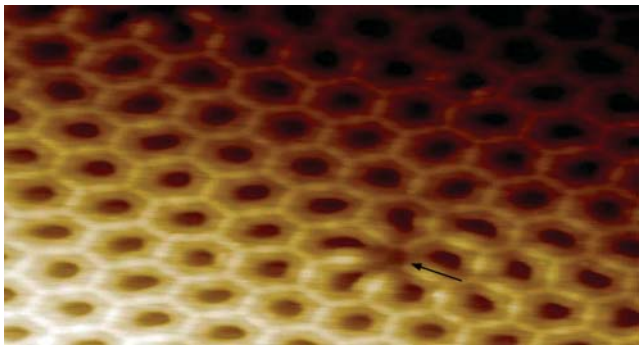

Figure 4. AFM image shows highly ordered hexagonal AAO nanopore structures, which are synthesized under carefully controlled anodization conditions using several steps. The interpore distance is 100 nm with a pore diameter of 30 nm. The arrow shows an asymmetric defect.

sisted of an 80:20 mixture of phosphoric acid and butanol at 60 °C to 65 °C with a potential of 10 V to 40 V. The current densities were limited to 30 mA/cm^2 to 50 mA/cm^2 (7).

Another consideration in the maximum theoretical limit of the porous layer thickness is the reaction kinetics that affects the chemical dissolution of the formed oxide layer. A realistic assessment of Equation 2 should consider the reversibility of the reaction. The forward and reverse equilibrium constants are temperature dependent. Moreover, for any specified temperature, the reaction consisting of pore formation and dissolution exists in a state of dynamic equilibrium. This effect was studied by Liechti and Treadwell, employing sulfuric acid and oxalic acid as the electrolytes (12). A maximum theoretical porous oxide formation rate of 20 μm/hour was estimated at a current density of 10 mA/cm^2.

Minimally controlled conditions during the anodization process typically produce nanoporous structures that contain imperfect pores. The pore walls do not contain a high degree of ordering and symmetry. Moreover, a large degree of variability in the pore diameter exists (Figure 3). Also note that the overall nanopore structure lies in the (001) plane, which is typical of cubic aluminum sheet that is generally used for commercial anodized aluminum applications.

The pore formation process, if performed under carefully controlled conditions, will produce highly ordered hexagonal structures containing near-perfect symmetry (Figure 4). This image was captured with an Agilent 5400 scanning probe microscope in AC-mode (tapping mode). When the instrument is configured in this mode, it is known as atomic force microscopy (AFM). The image provides details of the pore morphology only at the surface. AFM instruments typically assign dimensional parameters to captured images. The interpore spacing in Figure 4 is 100 nm with a pore diameter of 30 nm. The expected pore diameter is 10 nm for the specified anodization conditions. A post-anodization isotropic etch in 3% (V/V) chromic acid increased the pore diameter in preparation for the experimental synthesis of nickel nanowires with a nominal 30 nm diameter. This process and image exemplifies how nanoporous AAO has been used as a template for nanowire growth (13). Such controlled conditions are labor-intensive and do not readily allow the fabrication of inexpensive and easily produced nanostructures intended for sensing applications.

The controls imposed upon the synthesis process to generate highly ordered hexagonal nanopores entail a number of sequential steps (1, 3, 4, 7, 8, 14). Specifically, the aluminum that is employed as the base metal for the anodization process is typically of high purity (≥ 99.99%). The aluminum is annealed in such a way that the surfaces are aligned in the (100) orientation. Second, the base aluminum is electropolished using an acid-alcohol mixture at low temperatures to ensure that isotropic surface states are present. The

anodization is performed at low temperatures, typically 5 °C, with current densities at 10 mA/cm^2 to 20 mA/cm^2 for four hours. An isotropic etch, using 10% chromic acid, is employed to remove the initial oxide layer, exposing the dimpled aluminum surface. A second anodization process is performed for 24 hours or longer to generate the highly ordered hexagonal AAO matrix. Subsequent etching may be performed using a caustic base solution to remove the aluminum base material if necessary.

The synthesis of highly ordered hexagonal AAO nanopores using multi-step processes is not required for the manufacturing of the nanostructured sensor substrates. The process has entailed only a single-step anodization without the need for electropolishing (15). In the interest of commercial success and to economically mass produce the devices, controlling the single-step anodization parameters — for example, current density and temperature — has produced devices that meet the accuracy and repeatability benchmarks. Moreover, it is possible to employ vapor-deposited aluminum thin films with (111) orientation, rather than using the previously discussed (100) materials. The single-step anodization synthesis has been employed extensively in our investigation.

The exact pore-forming mechanism has never been understood. Attempts have been made to explain the mechanism in terms of the electric field distribution at the aluminum plane during the anodization process (6, 16, 17). A further attempt to explain the mechanism based upon ion migration has been published by Stanton and Golovin (14). The explanation entails assessing the electrochemical parameters using the Nernst-Planck equation to determine the flux of ions in solution and the Butler-Volmer relaxations to determine the flux at the liquid-metal interface (18). Upon establishing the flux densities, numerical methods involving computer simulation of the molecular orbital interactions were performed based upon quantum mechanical models. The resultant renderings of the simulations exhibited a good correlation to the hexagonal pore structures observed in the multi-step anodization process.

THIN-FILM DEPOSITION AND ANODIZATION

The initial fabrication work of the AAO thin films was performed at the Northern Illinois University Microelectronic Research and Development Laboratory (MRDL). The initial work entailed substrate preparation, metal deposition and surface analysis using AFM. The MRDL facilities contain several classes of cleanrooms, each specific to the scope of required device fabrication. The class-100 facilities were employed in this investigation to perform sputter deposition of metallic films. Anodization of the aluminum layer and subsequent analysis were performed outside of the MRDL environment.

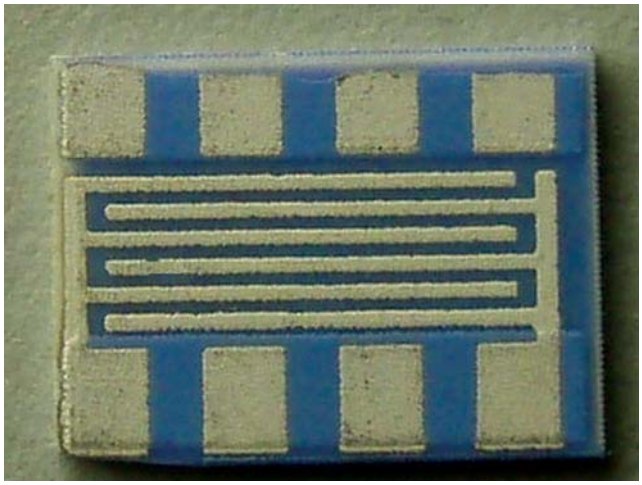

Figure 5. Planar view of finished AAO sensor. Sensor dimensions are 0.500 x 0.400 of an inch. Thin-film processing was employed to synthesize the underlying oxide layer; thick-film methods were used to pattern the electrodes and interconnects.

The synthesis process consisted of immersion cleaning a commercially manufactured ceramic substrate using isopropyl alcohol, rinsing in deionized water and drying in a nitrogen flow. The substrate serves as a rugged base material for deposition of overlying sensing elements and electrical interconnects. Deposition of a glass layer (SiO_2) is followed by standard screen-printing methods to apply insulating dielectric and conductor layers, which are required as interconnects serving as the electrical interface. For the sake of brevity, the electrical interface and electrical response of the device will not be discussed in this paper in order to maintain the focus on the surface characteristics. Moreover, because this work is a development of a sensor using (111) aluminum thin films, all aspects are considered to be an unexplored concept, and the response of the sensors are presented in the referenced publications (19-25). Figure 5 shows the finished chemical sensor complete with interdigitated surface electrodes and interface pads. The AAO appears as the blue-green semi-reflective surface; an overlying insulating layer appears as the light blue material.

A layer of 100 nm of titanium tungstide (TiW) was deposited on the SiO_2 surface. The TiW is conductive and provides an additional measure of adhesion for

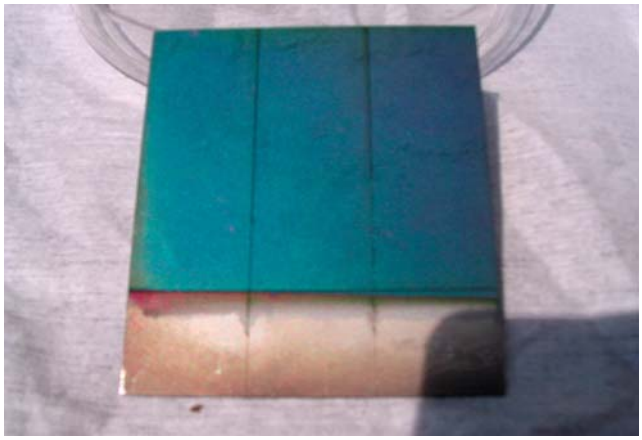

Figure 6. Planar view showing the AAO thin-film optical properties. The AAO film is a blue-green color when viewed perpendicular to the surface; it exhibits a color shift toward violet when viewed off-axis from perpendicular. The bright surface near the bottom is the non-anodized aluminum thin-film layer.

overlying metallic layers. As previously noted, the thick-film applied glass layer was provided to enhance the surface quality of the sintered ceramic substrate. Most vapor-deposited or sputtered metals do not readily adhere to oxides. The exceptions are gold (Au), chromium (Cr) and TiW. The TiW sputter target contained a stoichiometric composition of $Ti_{0.10}W_{0.90}$ as specified by the target manufacturer. The TiW deposition required 300 W for 30 minutes.

A layer of 1100 nm of Al was subsequently deposited over the TiW layer under the same plasma deposition conditions. Aluminum serves as the base metal for the sensor as it will be anodized in the subsequent operation. The Al deposition stage required 300 W for 90 minutes. Evaporated and plasma-deposited metals typically form islands of (111) domains during the deposition stage. This process of using (111) aluminum differentiates the work performed in this investigation from the work performed by Varghese (19, 21) and earlier investigators where (100) aluminum sheet was employed as the base metal for sensor applications.

Anodization of the aluminum surface was performed at 25 °C using 0.300 M oxalic acid at 40 V potential for 20 minutes. A platinum wire used as the cathode was formed in a 2 x 2-inch square shape to provide uniform current density. The power supply was set to constant current mode to limit the initial current to 220 mA providing 17 mA/cm^2 current density. A visual inspection of the anodized surface film in fluorescent and incandescent light rendered a typical optical thin-film response. Specifically, a gradual color change in the film's appearance occurred during the anodization process. The aluminum's shiny metallic luster changed to a dull white luster during the first 4 minutes, then to a green and subsequently to a violet-blue at the end-point. The substrates were removed from the electrolyte, rinsed in deionized water and dried in a nitrogen flow. The dry AAO samples exhibited typical scattering properties, where a slight color shift was observed depending upon the viewing angle relative to the incident light source. Viewed at an angle perpendicular to the surface, the color appears as blue-green (Figure 6). At angles approaching the tangent, the color appears violet.

SURFACE ANALYSIS

The surface morphology of the sputtered Al layer was analyzed using SEM and AFM. The SEM analysis at 10,000X magnification indicates granular domains (Figure 7). Closer inspection at 100.000X magnification shows the hexagonal grains (Figure 8). From this magnification, the average grain size appears as approximately 80 nm. Thin-film epitaxy using physical vapor deposition (PVD) methods, such as evaporation and sputtering, usually forms small islands or clusters of (111) domains as the materials deposit at nucleation sites on the substrate. These images exemplify the nucleation as the sputtered layer grows.

The anodized layer was analyzed to determine the surface characteristics. A simple resistance measurement using a two-point probe at locations along the oxide surface indicated that the oxide was of sufficient quality. In all instances, the DC resistance measured 1.5 MΩ, nominal at 1 cm distance between probes. A number of SEM measurements were performed using secondary electron detection to observe the surface oxide characteristics. At low magnification (50,000X), domains of crystallites can be observed (Figure 9), with the pores perceptible and appearing in an almost regular pattern. Further magnification at 100,000X shows two prevalent crystallographic orientations: tetragonal (111) and hexagonal (0001). From this SEM image, the average crystallite grain size appears to range from 200 nm to 300 nm (Figure 10). The size was estimated from the corresponding scale at the bottom right-hand side of the image.

Upon closer inspection at higher resolution (200,000X), the pores are highly visible on all surfaces and show irregularity at the "mouth," which is probably due to chemical etching while immersed in the electrolyte prior to rinsing (Figure 11). At maximum resolution (300,000X), more detail is observed (Figure

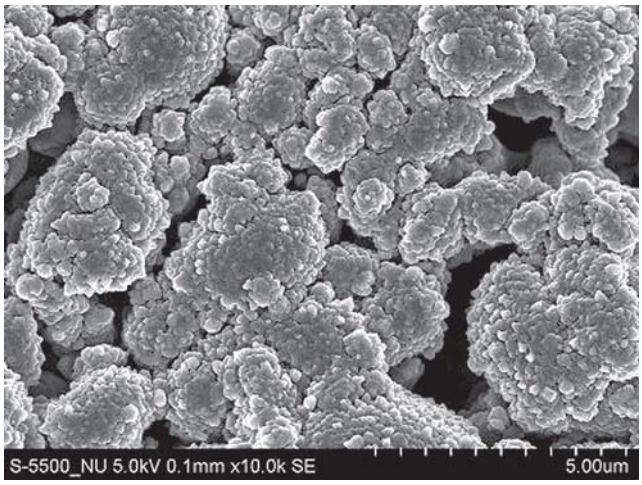

Figure 7. SEM image of sputtered aluminum grains at 10,000X magnification.

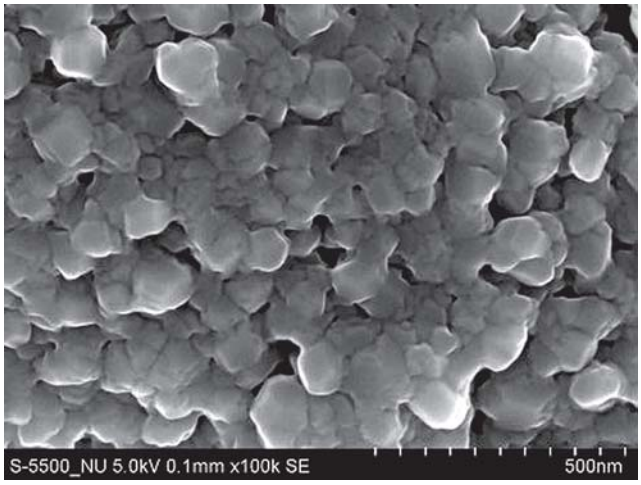

Figure 8. SEM image of sputtered aluminum grains at 100,000X magnification. The hexagonal grains are approximately 80 nm in diameter. Note the symmetry and regularity of the grains.

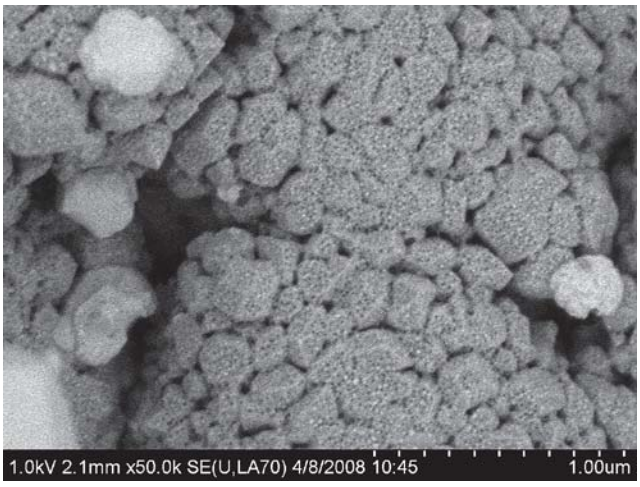

Figure 9. SEM image of AAO crystallites at 50,000X magnification.

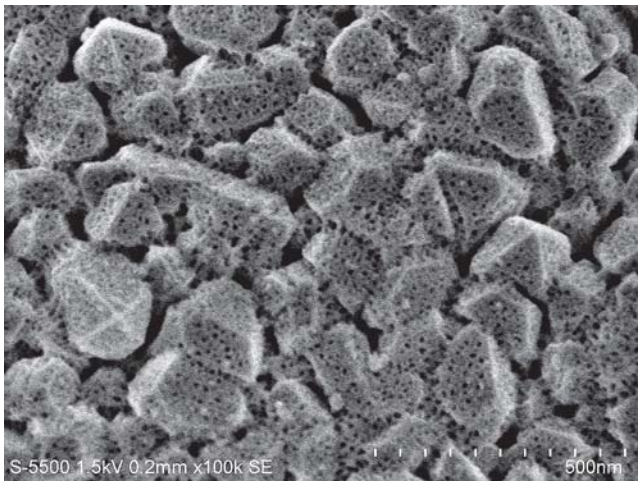

Figure 10. SEM image of AAO crystallites at 100,000X magnification.

12). Specifically, the cell walls may be discerned. The walls appear white and the interstitial regions appear as a grey shade. Using this image, an estimate may be made of the pore diameters and the cell thickness. The pore diameter appeared to be 10 nm and the cell thickness appeared to 18 nm to 20 nm. The cell thickness may also be determined by measuring the inter-pore distance, which is the center-to-center distance between pores. Moreover, equidistant spacing between pores is observed. The ratio of pore diameter to cell diameter determines the porosity. Here, the porosity may be greater than 50%.

Figure 9 was captured using the S-4800 SEM. At higher magnification, charging effects occurring in non-conductive materials becomes problematic. Several solutions exist to remedy this problem. One solution is to decrease the anode potential, which was decreased to 1.0 kV. The disadvantage to decreasing the potential is that resolution and image brightness will be sacrificed. The other viable solution is to sputter deposit or evaporate a small layer of carbon or gold onto the surface of the sample to enhance the conductivity, and therefore, dissipate the charge accumulation. Unfortunately, when working with nanostructured materials, the addition of metallic atomic layers will alter the surface and obscure the features that need to be studied. This is an example of Heisenberg's "uncertainty principle," which states that performing a measurement can alter the experiment, and altering the experiment can affect the measurement. The S-5500 SEM was employed for

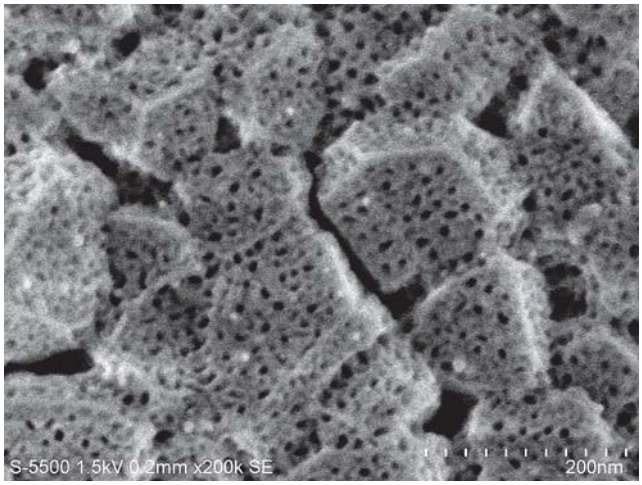

Figure 11. SEM image of AAO crystallites at 200,000X magnification.

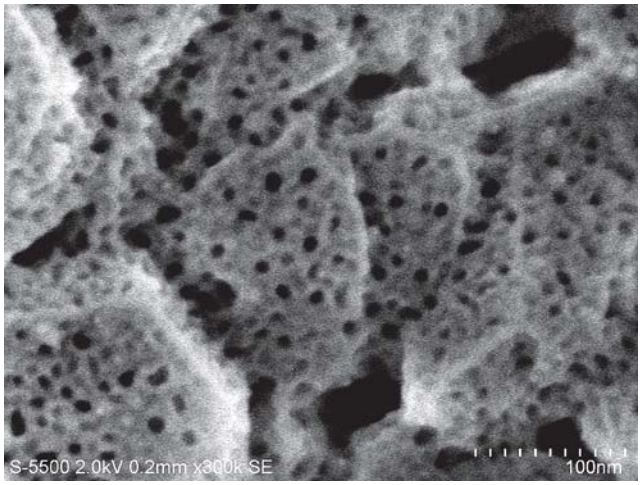

Figure 12. SEM image of AAO crystallites at 300,000X magnification. Cell porosity appears greater than 50%.

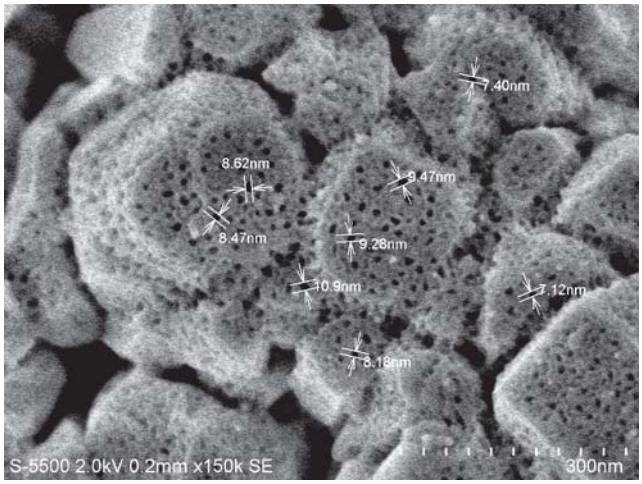

Figure 13. SEM image of AAO showing pore diameter measurements with built-in software tools. The average diameter is 9.1 nm.

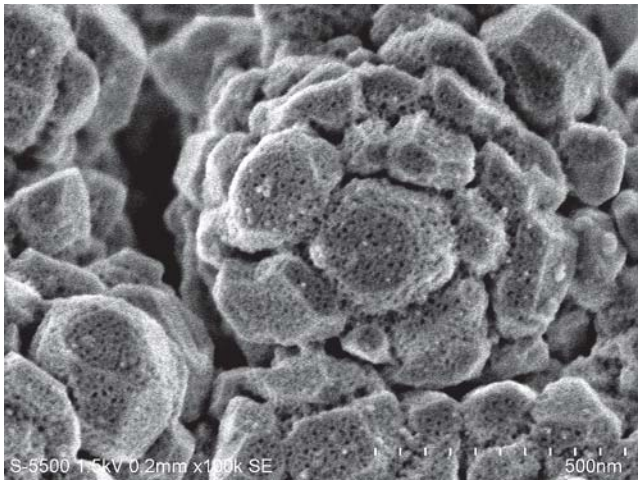

Figure 14. SEM image of AAO showing "rosebud" structure. Note the hexagonal macrostructure containing hexagonal and tetragonal crystallites.

subsequent imaging (Figures 10-14). The instrument was designed with enhanced low-angle detectors.

Precise pore diameter measurements were made using the S-5500 (Figure 13). The average pore diameter is 9.1 nm. This image also shows that the pores appear perpendicular to the grain surfaces. Pore formation and growth typically follow the macroscopic electric field assumed to emanate from the aluminum backplane during the anodization process and should be perpendicular to the sensor substrate surface rather than the lattice planes.

At a different region, the sample was imaged at lower magnification (100,000X). Interesting crystallite geometries were observed (Figure 14). A crystallite "rosebud" containing a hexagonal conglomeration of hexagonal grains was visible. Comparison of this image to Figure 7 shows the similarity of the aluminum islands before and after oxidation.

Atomic force microscopy was employed to obtain surface profile measurements. AFM instruments typically scan a square region with dimensions selected by the operator. The analog-to-digital (A/D) resolution is also user selectable. Several scans of the AAO were performed at various resolutions and sizes using a Quesant Q-350 high resolution AFM. The optimal imaging parameters were determined to be 1 μm square using 1024

bit A/D resolution (Figure 15). The image confirms the surface topology observed with the SEM such that the crystallites of various sizes and heights appeared. Statistical data were obtained using the signal processing tools inherent to the AFM depicted by the screen capture (Figure 16). A multimodal distribution appears such that three broad mean surface heights exist: 19 nm, 28 nm and 38 nm. A mean of 29.97 nm was calculated by the software to include the entire surface profile. The geometry of the AFM tip is such that the average diameter exceeds 10 nm. Hence, the nanopores observed in the SEM images cannot be deconvoluted.

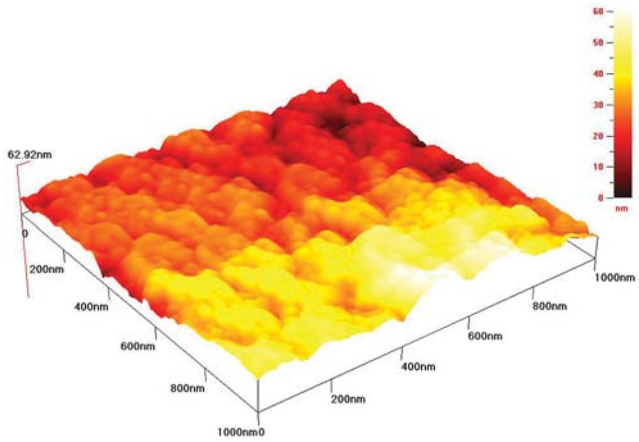

Figure 15. AFM image of a 1 µm square region of the AAO surface. The nominal crystallite domains are observed with false-color imaging to denote the surface profile in three dimensions.

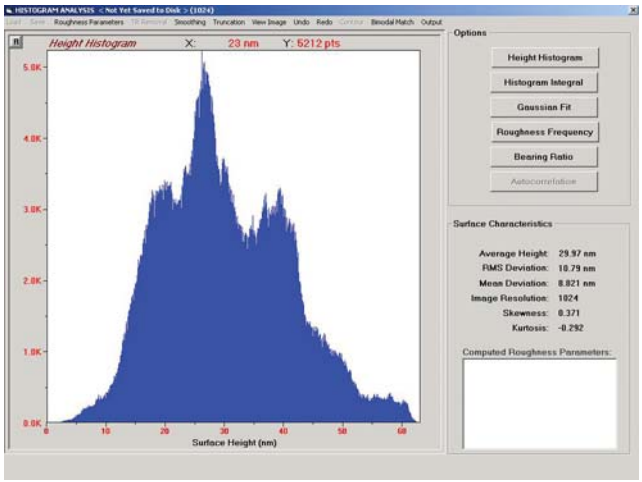

Figure 16. AFM software generates statistics of the AAO surface profile shown in this screen capture. Three overlapping Gaussian curves appear with means of 19 nm, 28 nm and 38 nm. The software calculated an overall average surface height of 29.97 nm.

DISCUSSION AND CONCLUSION

The extensive work performed by previous investigators during the early years of alumina research suggested that an amorphous gamma-alumina structure existed. The work performed during the past several decades, including this SEM investigation of these thin-film structures suggests that anodically synthesized material is not amorphous but contain regular repeating crystal units. As observed, the crystallites have a definite order and symmetry containing tetragonal and hexagonal geometries.

Reiterating the comparative differences in materials employed at the start of the synthesis process, vacuum-deposited (111) aluminum appears to form (111) and (1000) structures, and subsequently retains the crystallographic similarities when anodically oxidized. Moreover, the pore structures, when observed at high magnification, appear to grow radially outward from the crystal planes, rather than from the metallic substrate or backplane.

Subsequent work by our research group employed impedance spectroscopy to measure the dielectric properties of VOCs condensed on the surface and in the nanopore structure of the AAO sensors. We have found that the thin-film fabricated from (111) sputtered aluminum sensors exhibit an increased sensitivity to the VOCs when compared to the response of sensors fabricated from (100) or bulk aluminum sheet. The enhanced response is attributed to the increased surface area. From the SEM images it can be observed that there are many crystal planes containing nanopores. Therefore, there is a larger surface for the adsorption of VOCs to condense and an increased number of sites for molecular interactions to occur.

Future work by our group using the AAO materials entails several pathways. Specifically, we have observed that the adsorption and desorption times of VOCs is protracted due to the large size of the sensors. Rescaling of the sensors to a smaller overall area shows promise such that a fast measurement could occur. There is also interest in anchoring biological materials, including viral particles and antibodies, to the surface so that detection using electrical signatures could be performed.

The AAO material has a large bandgap of 11.4 eV. We are currently investigating the addition of dopants to the starting materials and the diffusion of dopants in the finished AAO materials in an effort to modify the bandgap so that semiconducting properties may be possible. The use of microscopy, particularly SEM

and EDS, will be necessary to study the surface morphology to determine how the dopants alter the crystal structure.

REFERENCES

1. Aluminum Association. "Anodic oxidation of aluminum and its alloys," *Information Bulletin*, **1**, pp 12-20, 1948.
2. Caboni. P. Italian Patent 339232, 1936.
3. Keller, F., Hunter, M.S. and Robinson, D.L. "Structural features of oxide coatings on aluminum," *Journal of the Electrochemical Society*, **100**, pp 411-419, 1953.
4. O'Sullivan, J.P. and Wood, G.C. "The morphology and mechanism of formation of porous anodic films on aluminum," Proceedings of the Royal Society A, **317**, pp 511-543, 1970.
5. Zoltai, T. and Stout, J.H. *Mineralogy: Concepts and Principles*, Burgess Publishing Co.: Minneapolis,1984.
8. Lide, D.R. *CRC Handbook of Chemistry and Physics*, 85th Edition, CRC Press, 2005.
6. Choi, J. "Fabrication of monodomain porous alumina using Nan imprinting lithography and its applications," In *Engineering*, Martin Luther Universitat-Halle: Wittenburg, Germany, pp 109, 2004.
7. Diggle, J.W., Downie, T.C. and Coulding, C.W. "Anodic oxide films on aluminum," *Chemical Reviews*, **69 (3)**, pp 365-405, 1969.
8. Jessensky, O., Muller, F. and Gosele, U. "Self-organized formation of hexagonal pore arrays in anodic alumina," *Applied Physics Letters*, **72 (10)**, pp 1173-1175, 1998.
9. Gorokh, G., Mozalev, A., Solovei, D., Khatko, V., Llobet, E. and Correig, X. "Anodic formation of low aspect ratio porous alumina films on metal oxide sensor application," *Electrochimica Acta*, **52 (4)**, pp 1771-1780, 2006.
10. Bosier, G., Pebere, N., Druez, C., Villatte, M. and Suel, S. "FESEM and EIS study of sealed AA2024 T3 anodized in sulfuric electrolytes: influence of tartaric acid," *Journal of The Electrochemical Society*, **155 (11)**, pp C521-C529, 2008.
11. Paolini, G., Masaero, M., Sacchi, F. and Pagnelli, J. "An Investigation of porous anodic oxide films on aluminum by comparative adsorption, gravimetric and electronoptical measurements," *Journal of The Electrochemical Society*, **112 (32)**, pp 32-38, 1965.
12. Liechti, F. and Treadwell, W.D. "The composition of electrolytic oxide layers on aluminum," *Helvetica Chimica Acta*, **30**, pp 1204-1218, 1947.
13. Masuda, H. and Fukuda, F. "Ordered metal nanohole arrays made by a two-step replication of honeycomb structures of anodic alumina." *Science*, **268**, pp 1466-1468, 1995.
14. Stanton, L.G. and Golovin, A.A. "Effect of ion migration on the self-assembly of porous nanostructures in anodic oxides," *Physical Review B*, **79 (035414)**, pp 1-7, 2009.
15. Chen, Z. and Lu, C. "Humidity sensors: a review of materials and mechanisms," *Sensor Letter*s, **3**, pp 274-295, 2005.
16. Patermarakis, G. and Karayannis, H.S. "The mechanism of growth of prorous anodic Al_2O_3 films on aluminum at high film thicknesses," *Electrochimica Acta*, **40**, pp 2647-2656, 1995.
17. Lee, W., Gosele, U. and Nielsch, K. "Fast fabrication of long-range ordered porous alumina membranes by hard anodization," *Nature*, **1038 (10)**, pp 741-747, 2006.
18. Bard, A.J. and Faulkner, L.R. *Electrochemical Methods*, Wiley and Sons: New York, 2001.
19. Varghese, O.K., Gong, D., Paulose, M., Ong, K.G. Grimes, C.A. and Dickey, E. C. "Highly ordered nanoporous alumina films: effect of pore size and uniformity on sensing performance," *Journal of Materials Research*, **17 (5)**, pp 1162-1171, 2002.
20. Haji-Sheikh, M., Andersen, M., and Ervin, J. "Anodic nanoporous humidity sensing thin films for commercial and applications," in the proceedings of the 39th IAS Annual Meeting, 2004.
21. Varghese, O.K., Gong, D., Dreschel, W.R., Ong, K.G. and Grimes, C.A. "Ammonia detection using nanoporous alumina resistive and surface wave sensors," *Sensors and Actuators B*, **94**, pp 27-35, 2003.
22. Radzik, C., Kocanda, M., Haji-Sheikh, M. and Ballantine, D.S. "Electrical impedance response of a thick-film hybrid anodic nanoporous alumina sensor to methanol vapors." *International Journal on Smart Sensing and Intelligent Systems*, **1 (2)**, pp 470-479, 2008.
23. Kocanda, M., Haji-Sheikh, M. and Ballantine, D.S. "Detection and discrimination of alcohol vapors using single-step anodized nanoporous alumina sensors," from the International Conference on Sensing Technology, Tianan, Taiwan, 2008.
24. Kocanda, M., Haji-Sheikh, M. and Ballantine D.S. "Detection of cyclic volatile organic compounds using single-step anodized nanoporous alumina sensors," *IEEE Sensors Journal*, **9 (7)**, pp 836-841, 2009.
25. Kocanda, M., Potluri, L., Haji-Sheikh, M., Bose, A. and Ballantine, D.S. "Enhanced Hydrogen Sensing Employing Electrodeposited Palladium Nanowires Enclosed in Anodized Aluminum Oxide Nanopores," from the IEEE Sensors Conference, Chirstchurch, New Zealand, 2009.